Experimental validation of synchronized Helix wake mixing control

van Vondelen, Aemilius A.W.; van der Hoek, Daan C.; Navalkar, Sachin T.; van Wingerden, Jan Willem

DOI
10.1016/j.renene.2025.124768

Publication date
2026

Document Version
Final published version

Published in
Renewable Energy

Citation (APA)
van Vondelen, A. A. W., van der Hoek, D. C., Navalkar, S. T., & van Wingerden, J. W. (2026). Experimental validation of synchronized Helix wake mixing control. *Renewable Energy*, *257*, Article 124768. https://doi.org/10.1016/j.renene.2025.124768

Renewable Energy 257 (2026) 124768

Contents lists available at ScienceDirect

Renewable Energy

journal homepage: www.elsevier.com/locate/renene

Experimental validation of synchronized Helix wake mixing control

Aemilius A.W. van Vondelen [a],*, Daan C. van der Hoek [a], Sachin T. Navalkar [b], Jan-Willem van Wingerden [a]

[a] Delft Center for Systems and Control, Delft University of Technology, Mekelweg 2, Delft, 2628 CD, The Netherlands
[b] Siemens Gamesa Renewable Energy B.V., Prinses Beatrixlaan 800, The Hague, 2595 BN, The Netherlands

ARTICLE INFO

Keywords:
Kalman filter
Wind turbine control
Wake mixing
Synchronization
Wind tunnel experiment

ABSTRACT

Wakes of upstream turbines impinge on downstream turbines in wind farms, causing power losses and increased fatigue. Wind farm control methods, such as the Helix approach, have been proposed to actively stimulate mixing of the wake with the free stream by pitching the blades dynamically. As a result, a periodic structure is forced in the wake, which increases average downstream wind velocity and thereby improves downstream turbines' power production. However, downstream turbines could further exploit this periodic wake structure by pitching dynamically as well, but in sync with the phase of the incoming wake structure. Depending on the phase offset between the impinging wake and the downstream pitch, this creates destructive or constructive interference between the two wakes and further improves power production downstream. This work presents and experimentally validates such a control strategy for downstream wind turbines and evaluates it on a three-turbine wind farm in an experimental wind tunnel setting using scaled wind turbines. Results validate the controller's effectiveness and show that the third turbine's performance improvement is strongly influenced by the phase offset between the periodic wake components generated by the second turbine and those present in the upstream wake.

1. Introduction

Wind energy serves as one of the main drivers towards the realization of a sustainable society. To reduce its cost, turbines are typically grouped in farms, allowing cabling, maintenance, and installation costs to be shared. The layout of such a farm primarily depends on the dominant wind directions [1]. Turbines are positioned so that their wakes minimally interact with downstream turbines, since such interactions significantly reduce performance and increase structural loading [2].

Situations in which turbines are waked occur relatively often [3]. Studies show that the power production decrease of offshore wind farms can be as high as 20%, with structural loading increasing similarly [4]. This indicates significant potential for wind farm control strategies that mitigate wake effects. Optimizing production and balancing loads at the farm level have received growing attention in recent years, where some turbines deviate from their individual optimum to benefit downstream turbines and enhance overall farm performance [5].

One elementary control method involves derating upstream turbines to preserve energy for downstream turbines [6]. Although not significantly enhancing performance, it may be used to distribute loads more evenly across turbines [7]. Wake steering appears more promising for performance increase and is already being adopted in state-of-the-art wind farms due to its simplicity and demonstrated Annual Energy Production (AEP) gains [1,8,9].

Another category of wind farm controllers promotes wake mixing with the surrounding ('free stream') wind field by dynamically manipulating the flow. Known as Dynamic Induction Control (DIC), this method collectively pitches blades sinusoidally to change the induction factor [10]. This causes flow immediately behind the turbine to mix effectively due to speed differences. This method, referred to as the 'Pulse', shows promising results in simulations, with higher pitch amplitudes yielding higher power gains. However, dynamic actuation increases fatigue loads, increasingly with pitch amplitude, especially on the tower and blades [11].

Dynamic Individual Pitch Control (DIPC) is a recent alternative to DIC [12]. Unlike collective blade actuation, DIPC applies a 120° phase shift to the actuation of each blade. This repositioning of the effective thrust center creates a helical wake shape, thus referred to as the 'Helix' approach [12].

The rotational direction of the Helix influences power gain, with counterclockwise (CCW) rotation typically superior to clockwise (CW)

---

* Corresponding author.
E-mail address: meesvanvondelen@live.nl (A.A.W. van Vondelen).

https://doi.org/10.1016/j.renene.2025.124768
Received 11 July 2025; Received in revised form 13 September 2025; Accepted 8 November 2025

rotation [12,13]. The Helix approach reduces thrust variations compared to the Pulse, adjusting only the thrust position rather than its magnitude. While blades experience slightly increased loads compared to the Pulse, tower loads significantly decrease [11]. Higher pitch amplitudes generally enhance performance but increase loads, especially on the pitch bearing [14,15].

The Helix approach enhances wake mixing by applying periodic tilt and yaw moments upstream, introducing periodic wake structures [11, 15]. These structures improve downstream turbine performance, but also introduce a periodic load downstream due to interaction with the impinging wake. Yet downstream turbines are operated without awareness of this periodicity induced upstream, which could either be regulated to reduce loads or enhanced to propagate the Helix wake further downstream. Our recent work first investigated feedback control for downstream turbines within a Helix wake to mitigate or reinforce this load, validated in large-eddy simulations (LES) [16].

Although LES provides valuable insights, it remains computationally intensive and sensitive to various modeling choices [5]. Lower-fidelity models reduce cost but introduce additional simplifications [2]. Practical challenges such as sensor noise and actuator limitations are typically not captured, motivating experimental validation under realistic conditions.

The potential of actively controlling downstream turbines in response to periodic wakes is largely unexplored. Earlier work indicates that the relative phase between downstream control inputs and periodic wakes strongly influences power production [17]. Aligning the up- and downstream wakes at any phase shift requires phase estimation techniques, as developed previously [18]. This is different compared to the approach developed in [16], which only allows load rejection or amplification.

Kalman filters effectively handle noise and provide unbiased estimates. Earlier work applied linear Kalman filters for wind speed estimation [19], whereas others employed an extended Kalman filter (EKF) for nonlinearities [20]. The linear approach requires multiple models for different conditions, whereas the EKF accommodates nonlinearities but introduces complexity. Typically, the wind speed is modeled as a random walk. However, this is generally not suited to estimating periodic wake dynamics [18].

Earlier work successfully explored an EKF synchronization approach for turbulent wake estimation, showing power improvements using nonlinear estimation in complex LES [21]. Moving beyond numerical validation, this study conducts the first experimental implementation in a controlled wind tunnel environment. Wind tunnel experiments provide high repeatability and precise inflow control, essential to validate estimator performance and synchronization impacts under realistic constraints.

A practical limitation is that the experimental setup lacks blade load sensors required for complex modeling approaches like blade element models [21]. Thus, a linear Kalman Filter relying solely on available strain measurements is adopted [18]. While less general, this approach is robust and computationally efficient for wind tunnel conditions.

Wind tunnels have validated wind farm control strategies effectively. Wake steering and closed-loop control have been demonstrated at Politecnico di Milano [22,23], while DIC and Helix control have been demonstrated at TU Delft [13,24]. Prior work attempted initial DIC wake alignment experiments without synchronization [25]. Experimental synchronization logically follows, bridging simulations and full-scale experiments.

This paper builds upon earlier theoretical and simulation studies [18,21], addressing the gap by experimentally validating synchronization in a scaled wind farm. The linear Kalman filter is adapted from previous frameworks [18] for the wind tunnel setting. Unlike prior studies, this paper develops practical estimator–controller integration, evaluates model accuracy, estimator repeatability, and quantifies phase offset impacts on performance, bridging theory and practical application.

The main contributions are:

1. **First experimental validation of synchronization:** Synchronization is validated within a three-turbine wind farm setup. The experiment assesses the ability of the downstream turbine to estimate the upstream wake phase and synchronize its control action.
2. **Adaptation of the synchronization control scheme:** Building upon the general synchronization framework proposed by [18], this study extends the method for integration with the wind turbine pitch control system.
3. **Quantification of optimal phase offset:** We identify the phase offset setting that maximizes power production at the third turbine. This provides valuable insights into the relationship between phase synchronization and downstream energy production.

The remainder of this paper is structured as follows. Section 2 revisits the theoretical framework for phase estimation using an augmented Kalman filter, and describes its integration with the wind turbine control system. Section 3 outlines the experimental setup used to evaluate the proposed scheme. System identification and estimator tuning are presented in Section 4, and the results are analyzed in Section 5. The paper concludes with a summary and recommendations in Section 6.

2. Estimation and control framework

This section first revisits the estimation framework introduced in [18], where a state-space model is augmented to include periodic inputs as additional states, enabling joint estimation of system states and periodic disturbances via a Kalman filter. The framework is then extended and connected to the wind turbine actuation system to enable real-time synchronization with the incoming periodic wake.

2.1. Deriving the augmented state-space model

To enable synchronization of the downstream turbine with the periodic wake-induced loading, it is necessary to estimate the phase and amplitude[1] of this disturbance in real time. However, the wake signal is not directly measurable. The strategy adopted here is to model the periodic wake forcing as a virtual input with known frequency but unknown amplitude and phase. By embedding this signal into the state-space system as an augmented state, its parameters can be estimated alongside the physical states using a Kalman filter. The derivation below formalizes this estimation structure.

A linear time-invariant (LTI) system with n states, r inputs, and m outputs is assumed:

$$\dot{x}(t) = Ax(t) + Bu(t), \tag{1}$$

$$y(t) = Cx(t) + Du(t), \tag{2}$$

where $x(t) \in \mathbb{R}^n$ denotes the state vector, $u(t) \in \mathbb{R}^r$ the input vector, $y(t) \in \mathbb{R}^m$ the output vector, and $\{A, B, C, D\}$ the system matrices of appropriate dimensions.

The state-space model described here represents the downstream turbine (T2), which uses wake estimation to synchronize its actuation. Although wind turbine dynamics are inherently nonlinear, the LTI assumption is considered acceptable in this context. This is because the experiments are conducted around a fixed operating point (constant wind speed and mean pitch angle), and the periodic forcing is performed at a single frequency. As such, the LTI model provides a sufficiently accurate approximation for use within the Kalman filter framework during these controlled wind tunnel experiments.

---

[1] Although the estimated amplitude is not used in the current control strategy, it could be leveraged to adapt the magnitude of the downstream turbine's pitch actuation in response to variations in upstream wake strength.

The inputs $u(t)$ are partitioned into controllable inputs $u^{\mathrm{c}}(t) \in \mathbb{R}^{r_c}$ and uncontrollable inputs $u^{\mathrm{u}}(t) \in \mathbb{R}^{r_u}$ such that $r = r_c + r_u$:

$$u(t) = \begin{bmatrix} u^{\mathrm{c}}(t) \\ u^{\mathrm{u}}(t) \end{bmatrix} + \begin{bmatrix} w^{\mathrm{c}}(t) \\ 0 \end{bmatrix}, \tag{3}$$

where $w^{\mathrm{c}}(t) \in \mathbb{R}^{r_c}$ is an input disturbance. Similarly, the input and feedthrough matrices are partitioned as:

$$B = \begin{bmatrix} B^{\mathrm{c}} & B^{\mathrm{u}} \end{bmatrix}, \quad D = \begin{bmatrix} D^{\mathrm{c}} & D^{\mathrm{u}} \end{bmatrix}. \tag{4}$$

The uncontrollable input $u^{\mathrm{u}}(t)$ primarily represents the environmental disturbances acting on the turbine, consisting mainly of the periodic component of the wake $u^{\mathrm{p}}(t) \in \mathbb{R}$, modeled as:

$$u^{\mathrm{p}}(t) = \sum_{i=1}^{h} \alpha_i \sin(\omega_i t + \varphi_i), \tag{5}$$

where α_i, φ_i, and ω_i are the amplitude, phase shift, and frequency of each periodic component, and h is the number of periodic components. Remaining uncontrollable disturbances are collected in $w^{\mathrm{u}}(t) \in \mathbb{R}^{r_u}$:

$$u^{\mathrm{u}}(t) = \begin{bmatrix} u^{\mathrm{p}}(t) \\ 0 \end{bmatrix} + w^{\mathrm{u}}(t). \tag{6}$$

Since an estimate of $u^{\mathrm{p}}(t)$ will be used for control, it is modeled as a periodic disturbance acting through the controllable actuators for estimation simplicity. Although the physical wake disturbance enters the system through unknown pathways (B^{u}), estimation is performed by reconstructing the disturbance effect in terms of the known controllable input channels (B^{c}). This is justified because the objective is to recreate the turbine's response rather than model the true disturbance path. Representing the periodic wake-induced loads as equivalent control actions allows accurate estimation and control synthesis without requiring identification of the matrix B^{u}.

To express the periodic input in state-space form suitable for Kalman filtering, we define the disturbance state vector as:

$$x^{\mathrm{p}}(t) = \begin{bmatrix} \alpha_1 \sin(\omega_1 t + \varphi_1) \\ \alpha_1 \cos(\omega_1 t + \varphi_1) \\ \vdots \\ \alpha_h \sin(\omega_h t + \varphi_h) \\ \alpha_h \cos(\omega_h t + \varphi_h) \end{bmatrix}, \tag{7}$$

so that:

$$u^{\mathrm{p}}(t) = \begin{bmatrix} 1 & 0 & \dots & 1 & 0 \end{bmatrix} x^{\mathrm{p}}(t), \tag{8}$$

$$u^{\mathrm{p}\dagger}(t) = \begin{bmatrix} 0 & 1 & \dots & 0 & 1 \end{bmatrix} x^{\mathrm{p}}(t), \tag{9}$$

where $u^{\mathrm{p}\dagger}(t)$ represents the quadrature (90-degree phase-shifted) component. The dynamics of $x^{\mathrm{p}}(t)$ follow as:

$$\dot{x}^{\mathrm{p}}(t) = A^{\mathrm{p}} x^{\mathrm{p}}(t), \tag{10}$$

where:

$$A^{\mathrm{p}} = \mathrm{diag}(\Omega_1, \dots, \Omega_h), \quad \Omega_i = \begin{bmatrix} 0 & \omega_i \\ -\omega_i & 0 \end{bmatrix}. \tag{11}$$

The periodic excitation frequencies ω_i are assumed to be known a priori from the upstream turbine actuation. Intuitively, the augmented states act as a virtual harmonic oscillator embedded within the system. As this oscillator evolves at the known excitation frequency, its phase and amplitude adjust to match the unmeasured periodic disturbance. This enables the Kalman filter to estimate the disturbance's effect on the system in real time, even though the forcing itself is not directly observable.

The mapping from the periodic disturbance states to the control inputs is achieved by introducing selection matrices. Specifically, the disturbance matrices are constructed as:

$$B^{\mathrm{p}} = B^{\mathrm{c}} V, \quad D^{\mathrm{p}} = D^{\mathrm{c}} V, \tag{12}$$

where

$$V = \begin{bmatrix} V_1 & V_2 & \dots & V_h \end{bmatrix}, \tag{13}$$

and each $V_i \in \mathbb{R}^{r_c}$ is a selection vector containing zeros except for a single one at the position corresponding to the control input through which the ith periodic disturbance acts. This structure ensures that each periodic input component is associated with a specific control channel while maintaining flexibility for multi-input extensions.

The continuous-time system from Eqs. (1)–(2) augmented with the disturbance model is now given by:

$$\begin{bmatrix} \dot{x}(t) \\ \dot{x}^{\mathrm{p}}(t) \end{bmatrix} = \begin{bmatrix} A & B^{\mathrm{p}} \\ 0 & A^{\mathrm{p}} \end{bmatrix} \begin{bmatrix} x(t) \\ x^{\mathrm{p}}(t) \end{bmatrix} + \begin{bmatrix} B^{\mathrm{c}} \\ 0 \end{bmatrix} u^{\mathrm{c}}(t) + \begin{bmatrix} w(t) \\ 0 \end{bmatrix}, \tag{14}$$

with corresponding output equation:

$$y(t) = \begin{bmatrix} C & D^{\mathrm{p}} \end{bmatrix} \begin{bmatrix} x(t) \\ x^{\mathrm{p}}(t) \end{bmatrix} + D^{\mathrm{c}} u^{\mathrm{c}}(t) + v(t). \tag{15}$$

The augmented system is then discretized using a zero-order hold assumption at the controller sampling rate, yielding the discrete-time system matrices $A_{\mathrm{d}}, B_{\mathrm{d}}, C_{\mathrm{d}}, D_{\mathrm{d}}$.

2.2. Connecting the wind turbine control system

The model is now connected to the turbine actuation system. Each blade ($i = 1, 2, 3$) can be actuated through its pitch angle $\theta_i(t)$. Blade root moments $M_i(t)$ can be measured. Due to coupling through the rotor, a multi-blade coordinate (MBC) transformation [26] is applied to decouple the system into collective, tilt, and yaw components (Fig. 2). The backward MBC transform is:

$$\begin{bmatrix} \theta_1(t) \\ \theta_2(t) \\ \theta_3(t) \end{bmatrix} = \begin{bmatrix} 1 & \cos(\psi_1) & \sin(\psi_1) \\ 1 & \cos(\psi_2) & \sin(\psi_2) \\ 1 & \cos(\psi_3) & \sin(\psi_3) \end{bmatrix} \begin{bmatrix} \theta_0(t) \\ \theta_{\mathrm{tilt}}(t) \\ \theta_{\mathrm{yaw}}(t) \end{bmatrix}, \tag{16}$$

where ψ_i denotes the blade azimuth.

Helix control operates in this frame by prescribing sinusoidal tilt and yaw signals as:

$$\theta_{\mathrm{tilt}}(t) = a_h \sin(\omega_{\mathrm{e}} t), \tag{17}$$

$$\theta_{\mathrm{yaw}}(t) = a_h \sin(\omega_{\mathrm{e}} t \pm \pi/2), \tag{18}$$

with a_h the amplitude, ω_{e} the angular frequency, and the phase shift ($+\pi/2$ for CCW helix, $-\pi/2$ for CW). The angular frequency ω_{e} is governed by the dimensionless Strouhal number, which characterizes oscillating flow dynamics and is defined as the ratio of a characteristic frequency to the flow speed and a relevant length scale:

$$\mathrm{St} = \frac{f_{\mathrm{e}} D}{U}, \tag{19}$$

where $f_{\mathrm{e}} = \omega_{\mathrm{e}}/2\pi$ is the excitation frequency in Hz, D is the turbine rotor diameter, and U is the free stream wind speed. Previous studies have found Strouhal values between 0.2–0.4 to be optimal for wake mixing [13]. See Fig. 1 for a visualization of the Helix wake.

Similarly, blade root moments are mapped via the forward MBC transform:

$$\begin{bmatrix} M_0(t) \\ M_{\mathrm{tilt}}(t) \\ M_{\mathrm{yaw}}(t) \end{bmatrix} = \frac{2}{3} \begin{bmatrix} 0.5 & 0.5 & 0.5 \\ \cos(\psi_1) & \cos(\psi_2) & \cos(\psi_3) \\ \sin(\psi_1) & \sin(\psi_2) & \sin(\psi_3) \end{bmatrix} \begin{bmatrix} M_1(t) \\ M_2(t) \\ M_3(t) \end{bmatrix}. \tag{20}$$

A graphical representation of the fixed coordinate frame can be seen in Fig. 2.

To connect the abstract state-space model to the physical turbine system, we identify the controllable input vector $u^{\mathrm{c}}(t)$ with the tilt and yaw components of the MBC-transformed pitch actuation:

$$u^{\mathrm{c}}(t) = \begin{bmatrix} \theta_{\mathrm{tilt}}(t) \\ \theta_{\mathrm{yaw}}(t) \end{bmatrix}. \tag{21}$$

Similarly, the system output $y(t)$ consists of the measured blade root moments in the tilt and yaw directions:

$$y(t) = \begin{bmatrix} M_{\mathrm{tilt}}(t) \\ M_{\mathrm{yaw}}(t) \end{bmatrix}. \tag{22}$$

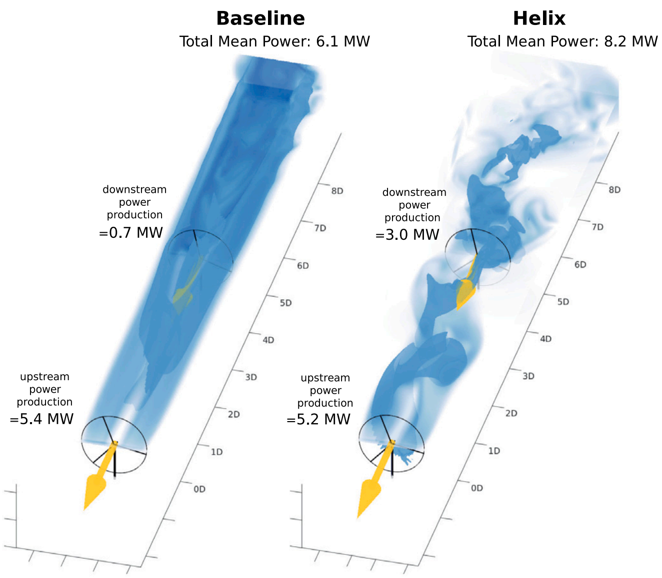

Fig. 1. Visualization of the baseline (left) and Helix-controlled (right) cases in a two-turbine array under full wake overlap. The data is based on a Large-Eddy Simulation with laminar inflow conditions by [12], and the image is adapted from [5]. Turbine spacing along the x-axis is normalized by rotor diameter D.

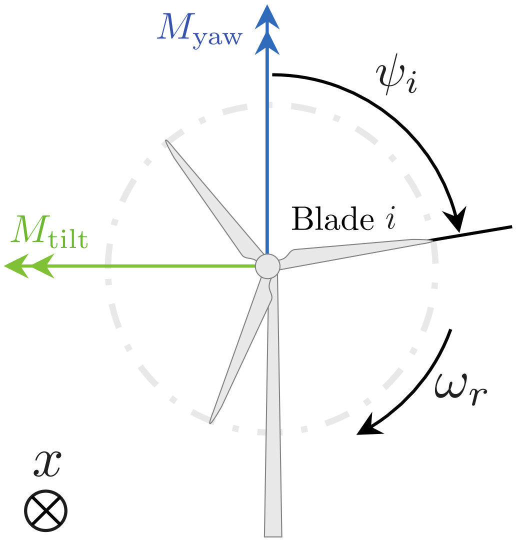

Fig. 2. Graphic representation of blade azimuth ψ_i and associated sign convention for tilt and yaw moments M_{tilt} and M_{yaw}.

These quantities are obtained by applying the MBC transformations (Eqs. (16) and (20)) to the individual blade signals. This mapping grounds the abstract model in measurable and actuated quantities on the real turbine, enabling state estimation and control in the rotating frame.

In the current experimental setup, however, only the fore–aft strain at the tower base is available as a measurement, which serves as a proxy for the tilt moment $M_{\text{tilt}}(t)$. No sensors are available to measure yaw-related loads or moments. As a result, system identification is performed on a single-input single-output (SISO) basis, considering only the tilt pitch input and the corresponding fore–aft strain output. This restriction simplifies the estimator implementation and focuses the phase estimation on the tilt component of the wake, which is sufficient due to the orthogonality of the tilt and yaw modes. The system output $y(t)$ is therefore limited to the fore–aft strain measurement, and the control input $u^{\text{c}}(t)$ is restricted to $\theta_{\text{tilt}}(t)$ in the present implementation.

2.3. Phase extraction and synchronization

After Kalman filter estimation, the periodic states $\hat{x}_k^{\text{p}}$ are available (this step is not described here; any conventional Kalman filter method for state estimation suffices, see e.g., [27]). The instantaneous phase $\phi_{i,k}$ of each periodic component i can be extracted as:

$$\phi_{i,k} = \operatorname{atan2}\left(\hat{x}^{\text{p}}_{2i-1,k}, \hat{x}^{\text{p}}_{2i,k}\right). \tag{23}$$

The control action for the downstream turbine is synthesized as:

$$u^{\text{c}}_{i,k} = a_i \sin(\phi_{i,k} + \varphi_{\text{off}}), \tag{24}$$

where a_i is the desired actuation amplitude and φ_{off} a desired phase shift for synchronization. A schematic of the proposed control scheme is displayed in Fig. 3.

2.4. Interpretation of φ_i

In the disturbance model of Eq. (5), the phase offset φ_i represents the initial phase shift of the ith periodic component relative to a sine reference at $t = 0$. In practice, φ_i can be inferred from the estimated instantaneous phase $\phi_{i,k}$ and the known excitation frequency ω_i according to:

$$\varphi_i \approx \phi_{i,k} - \omega_i t_k, \tag{25}$$

where t_k is the time at step k. This allows phase differences to be computed in real time without requiring prior knowledge of the initial phase φ_i, as the estimator continuously tracks the phase from measurement data. Although the control algorithm directly uses the time-varying phase estimate $\phi_{i,k}$, the results section (Section 5) analyzes the inferred constant offset φ_i to better compare phase relationships across different cases.

2.5. Summary

In summary, the proposed estimation framework integrates the periodic disturbance as an augmented state, enabling real-time estimation of its phase through a Kalman filter. By leveraging a known excitation frequency and mapping the disturbance effect through the controllable actuators, the method avoids the need to identify the true disturbance path. This provides a more effective and straightforward solution for downstream wake synchronization control.

3. Experimental setup

This section presents the experimental setup for evaluating the control scheme presented in the previous section. A description of the wind tunnel, wind turbine, and wind turbine control system is provided.

3.1. Wind tunnel

The experiments were conducted in the Open Jet Facility (OJF) at the Faculty of Aerospace Engineering, Delft University of Technology. The OJF is a closed-circuit, open-jet wind tunnel with an octagonal outlet measuring 2.85 m × 2.85 m. It has a contraction ratio of 3:1 and is capable of reaching a free-stream velocity of up to 35 m/s, with a turbulence intensity (TI) between 0.5% and 2% [28]. Unlike conventional closed-section wind tunnels, the open-jet setup minimizes wall interference, allowing for more representative wake and flow interaction studies. The current experiments were conducted at a free-stream velocity of $U = 6$ m/s. See Fig. 4 for a schematic of the setup in the wind tunnel.

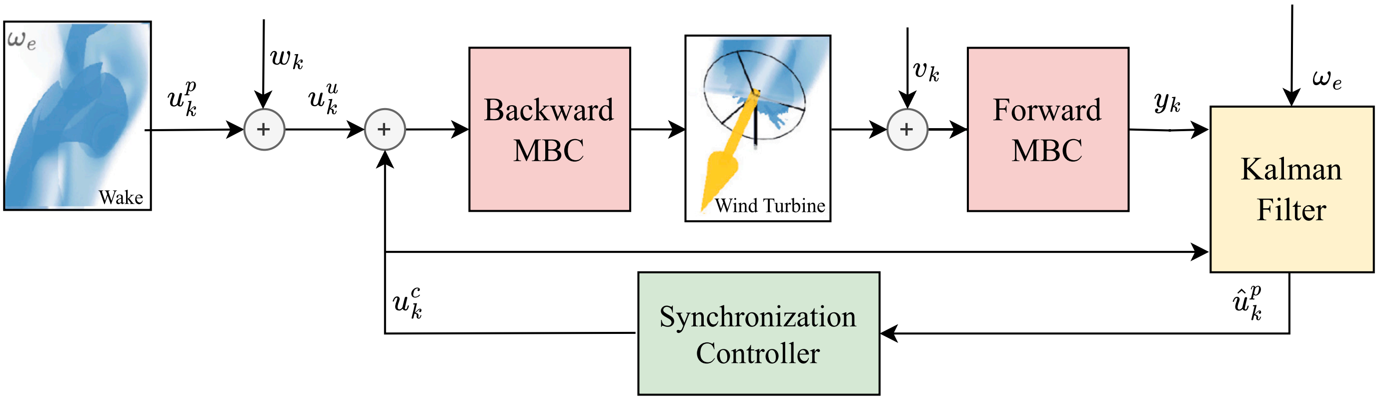

Fig. 3. Schematic of the proposed control scheme.

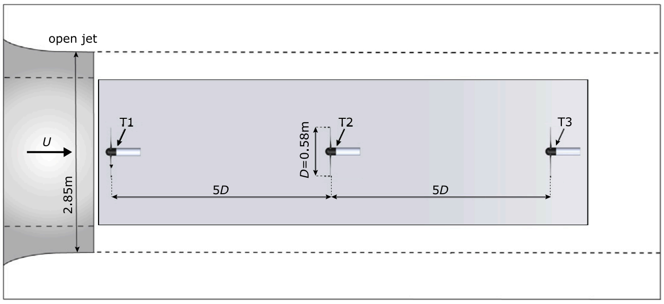

Fig. 4. Schematic of the experimental setup in the OJF. U denotes the free stream wind speed, D the turbine rotor diameter, and $T1$, $T2$, $T3$ denote turbines 1 to 3.

3.2. Wind turbine

The experiment used three modified MoWiTo-0.6 scaled three-bladed wind turbines developed at Oldenburg University [29] (see Fig. 5). Each turbine has a rotor diameter of 0.58 m and is equipped with a generator for torque control and a collective pitch control system.

Due to the small rotor size, the required Helix excitation frequency f_e is significantly higher than for utility-scale turbines. For example, compared to a modern 200 m rotor turbine, the actuation frequency is about 345 times larger (see Eq. (19)). This leads to stronger unsteady aerodynamic effects such as dynamic stall and lift hysteresis, resulting in greater production losses [30]. Previous experiments showed power losses of 10%–15% on turbines applying Helix control [13], while utility-scale turbines only see marginal losses in LES [15].

Although the Helix excitation is applied at a fixed-frame frequency f_e, the MBC transformation shifts this in the rotating frame, interacting with the 1P frequency. The resulting blade-level frequency becomes $1P + f_e$ (CCW) or $1P - f_e$ (CW) [26]. For instance, at $U = 6$ m/s, 1P is around 16.5 Hz and f_e is 2.5 Hz, resulting in an effective 19 Hz actuation frequency for CCW Helix.

To avoid demanding high actuator bandwidth, a swashplate mechanism is used. Three stepper motors in the fixed frame actuate a static ring, which transfers motion to the rotating hub via a ball-bearing system, emulating IPC (see Fig. 6 for a render of this mechanism). Tilt and yaw pitching modes are generated using a Clarke transform [31]:

$$\begin{bmatrix} \theta_a \\ \theta_b \\ \theta_c \end{bmatrix} = \begin{bmatrix} 1 & 1 & 0 \\ 1 & -1/2 & \sqrt{3}/2 \\ 1 & -1/2 & -\sqrt{3}/2 \end{bmatrix} \begin{bmatrix} \theta_0(t) \\ \theta_{\text{tilt}}(t) \\ \theta_{\text{yaw}}(t) \end{bmatrix}. \tag{26}$$

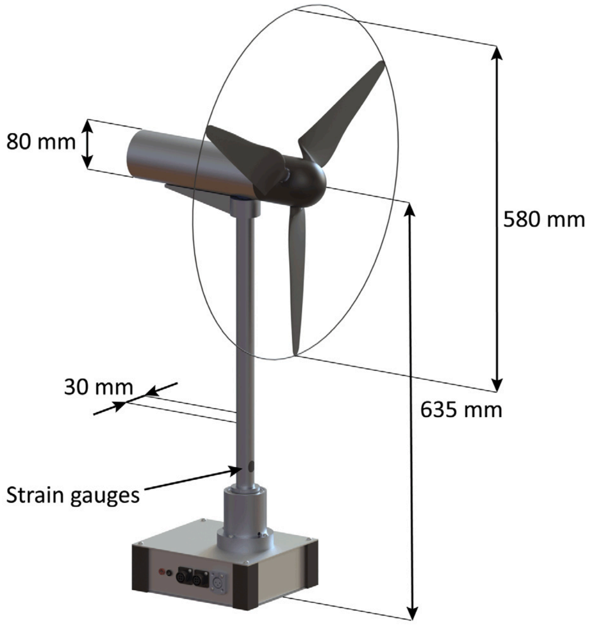

Fig. 5. Illustration of the MoWiTo-0.6 scaled wind turbine and its dimensions and strain gauge location.

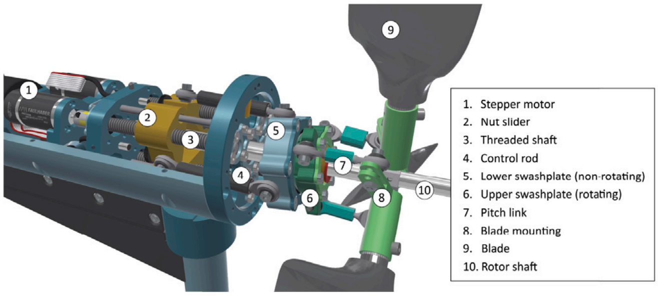

Fig. 6. Render of the internal components of the MoWiTo-0.6 turbine with the modified swashplate mechanism. The swashplate enables IPC by translating low-frequency actuation in the fixed frame into cyclic pitching of the rotating blades, thereby facilitating implementation of the Helix control strategy at reduced actuation bandwidth requirements [13].

In this setup, the collective pitch angle $\theta_0(t)$ is fixed at 10° to maintain operation near the optimal aerodynamic point. Only tilt and

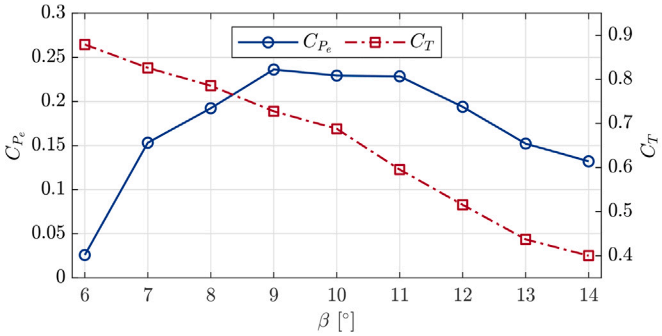

Fig. 7. Characterization of the aerodynamic coefficients of the MoWiTo-0.6 turbine for the optimal tip-speed ratio of 5.5. Note the sharp decline of C_{P_e} for small deviations from the optimal pitch angle [32].

Table 1
Summary of the evaluated cases.

Case	T1	T2	T3
BL Helix	Helix	Greedy	Greedy
Cases	Helix	Sync Helix + 0:30:330 deg	Greedy

yaw modes are dynamically varied. The third turbine (T3) operates with greedy (non-synchronized) control.

Measurements include pitch angle, rotational speed, and generator current. Additionally, strain gauges were installed at the tower base to measure fore–aft strain, which serves as a proxy for the tilt moment. Blade root sensors were not available. As tilt and yaw modes are orthogonal, estimating only tilt is sufficient. All measurements and control commands are exchanged via a dSPACE MicroLabBox.[2]

In prior work [32], the aerodynamic coefficients C_{P_e} and C_T were characterized. At a tip-speed ratio of 5.5 and collective pitch of 10°, the turbine achieves maximum power. Fig. 7 shows that even small pitch deviations reduce C_{P_e} significantly. However, because the collective pitch remains constant here, the main source of loss is unsteady aerodynamics like dynamic stall. This behavior is more pronounced in scaled turbines due to sharper C_P peaks, while full-scale turbines are more robust thanks to higher Reynolds numbers. Torque control uses a standard $K\omega^2$ law.

3.3. Experiments

Each experimental trial begins with a baseline (BL) Helix case: Turbine 1 (T1) operates under Helix control, while Turbines 2 and 3 (T2 and T3) use greedy control. This establishes the reference performance level.

Next, a series of synchronization cases is executed, where T2 applies synchronized Helix control with a prescribed phase offset φ_{off}, selected from the set $\{0°, 30°, \ldots, 330°\}$ in randomized order. T1 continues applying its Helix signal throughout the trial, while the Kalman filter estimation in T2 is reinitialized at each case. Each trial concludes with a second BL Helix case. Power and load results from the first and last BL cases are averaged to correct for startup effects and drift.

In total, 14 experiment trials and 3 validation trials were conducted. In the validation trials, T2 performs phase estimation but does not apply control, allowing assessment of estimator performance alone. Each case lasts 90 s, followed by a 15-second transition. Fig. 8 and Table 1 summarize the evaluated scenarios.

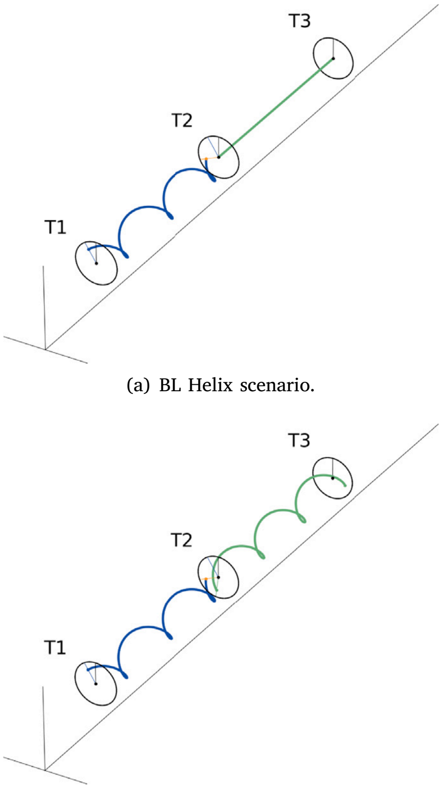

(a) BL Helix scenario.

(b) Synchronization.

Fig. 8. Schematic representation of the evaluated cases. In the baseline (BL) Helix scenario, only the upstream turbine (T1) applies Helix control. In the synchronization scenario, both T1 and T2 apply Helix control, with wake structures phase-aligned. T3 operates under baseline control.

4. System identification and tuning

Reliable performance of the Kalman-filter-based synchronization scheme requires an accurate linear model of the downstream turbine. Input–output data were collected at steady operating conditions using pseudo-random binary noise (PRBN) excitation. Subspace identification yielded a 5-state linear model that captures the turbine dynamics in the frequency range relevant for Helix synchronization (0.2–5 Hz). Model accuracy was confirmed by comparing the frequency response to experimental data (Fig. 9), with good agreement near the excitation frequency. Further details of the identification procedure, model order selection, and validation are provided in Appendix A.

For Kalman filter tuning, process and measurement noise covariances were set heuristically based on repeated trials. Identified states were assigned low process noise, while augmented disturbance states were given adjustable noise to balance sensitivity and robustness. Measurement noise was set conservatively low, reflecting high sensor precision. This yielded stable convergence and consistent phase estimation across experiments. Full tuning details are given in Appendix A.

5. Results

This section presents the experimental results. The goal is to evaluate whether the downstream turbine can reliably estimate the phase of the incoming periodic wake *and* whether synchronized control based on that estimate improves performance. The results are grouped into three parts:

---

[2] https://www.dspace.com/en/inc/home/products/hw/microlabbox.cfm.

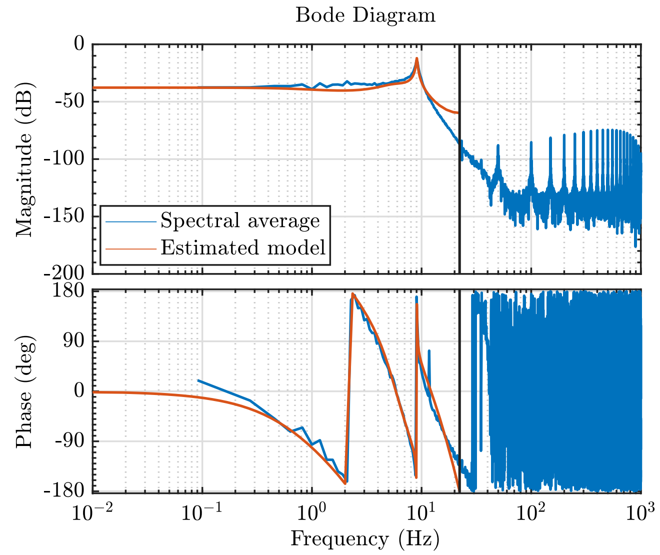

Fig. 9. Frequency response comparison between the identified 5-state linear model and measured experimental data.

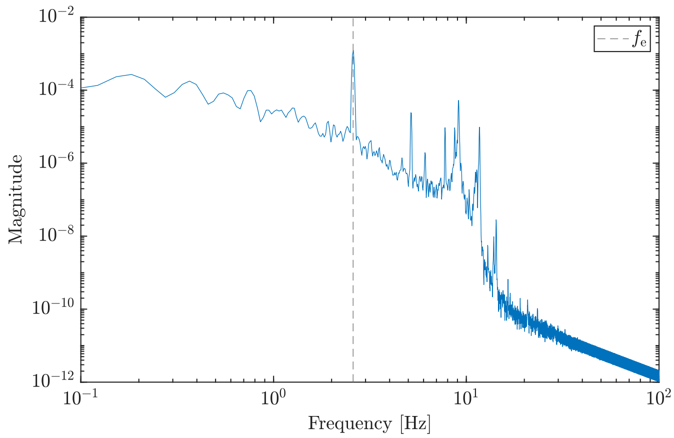

Fig. 10. Power spectrum of the tower-base strain signal at the downstream turbine. A dominant peak appears at the helix excitation frequency f_e.

- Estimator validation, which verifies that the periodic wake can be detected in the measurements and that the estimator tracks its phase consistently.
- Repeatability analysis, which assesses how the estimated phase varies across multiple trials and under different synchronization settings.
- Synchronization performance, which analyzes how applying different phase offsets in the downstream turbine affects the power production of both that turbine and the one behind it.

5.1. Estimator validation

The first step in validating is to check whether the estimator can correctly detect the phase of the periodic upstream wake. Earlier studies [11,16] showed that helix control creates a repeating wake pattern that appears in the strain measurements of the downstream turbine.

Let us first confirm that this periodic structure can be found in the measurement. Fig. 10 shows the frequency content of the strain signal at the tower base of the downstream turbine. A clear peak is seen at the excitation frequency f_e, confirming the periodic nature of the wake and its presence in the measured signal.

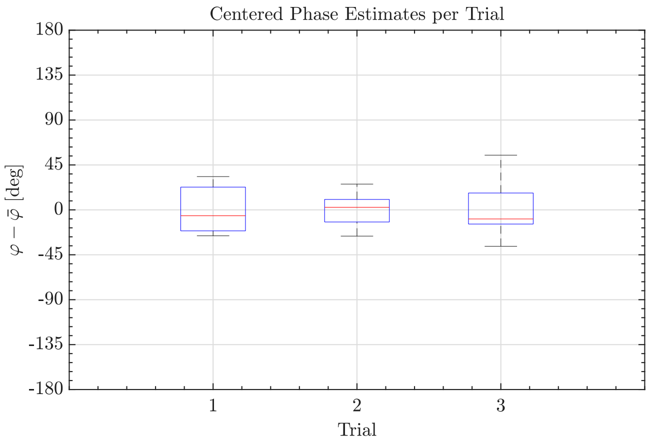

Fig. 11. Box plot of phase estimates from three open-loop trials. Each estimate was adjusted by subtracting the trial's average $\bar{\varphi}$. The central red mark is the median, the bottom and top edges of the box are the 25th and 75th percentiles, respectively, and the whiskers denote the highest and lowest points not considered outliers.

Now we need to test if the estimator can detect this signal and its phase consistently. To assess this, we conducted three open-loop trials, each consisting of 12 repetitions of the BL Helix case under identical inflow and upstream actuation conditions. In each case, the estimated phase shift was tracked over time, and a linear fit was applied to the unwrapped signal to extract a representative steady-state phase offset. Note that at this stage, we do not yet apply a control action to the downstream turbine, but only estimate the phase of the incoming wake (BL Helix case).

Let us now investigate the estimated phase shift results across the three trials. Because phase angles wrap around (e.g., 179° and −179° represent nearly the same direction), we used a method that accounts for this when computing the average phase shift in each trial. Also, the absolute phase values vary between trials. This is likely caused by small differences in how the Kalman filter was initialized in each trial. Because the estimator updates its prediction step by step, any small error at the initialization can continue throughout the whole trial. While this does not affect the overall trend within a single trial, it can shift the baseline of the estimated phase when comparing different trials. To better compare the spread of estimates, we therefore subtracted the average phase shift of the entire trial, $\bar{\varphi}$, from each individual estimate and wrapped the result to the interval $[-180°, 180°]$. This gives a clear view of how much each estimate differs from the trial's average $\bar{\varphi}$, without being affected by angle wrapping.

Fig. 11 presents the centered phase estimates using box plots. Each box indicates the 25th to 75th percentile, illustrating the spread of estimates within each trial. The spread is observed to be reasonable and consistent across all three validation trials, indicating stable estimator performance. To further assess the distribution, Fig. 12 shows a histogram of all centered phase estimates combined from the three trials, revealing a clear peak near zero and a symmetric distribution, suggesting unbiased estimation. Having established the reliability of the estimator in this open-loop setting, we now transition to the closed-loop scenario, where the estimated wake phase is used in real time to apply synchronized Helix control commands on the downstream turbine (T2).

5.2. Repeatability of estimated phase across trials

The next experiment tested the estimator under active control, where different phase offsets were applied to the downstream turbine. The goal was to evaluate how the estimator performs when the downstream turbine itself changes due to actuation.

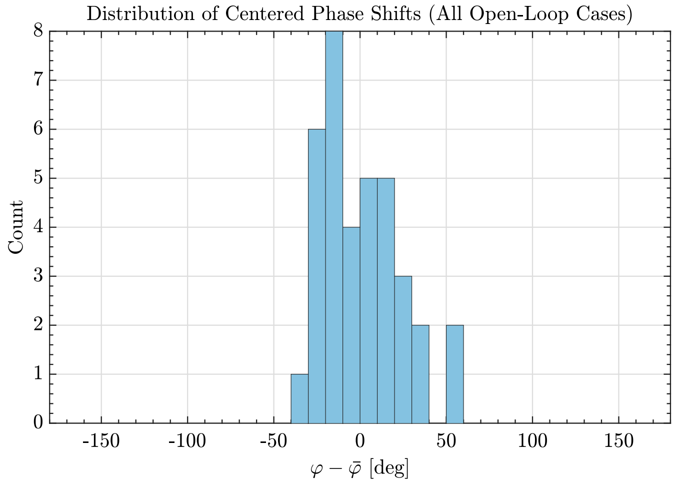

Fig. 12. Histogram of centered phase estimates across all three open-loop trials. The narrow spread demonstrates repeatability of the estimator under identical flow conditions.

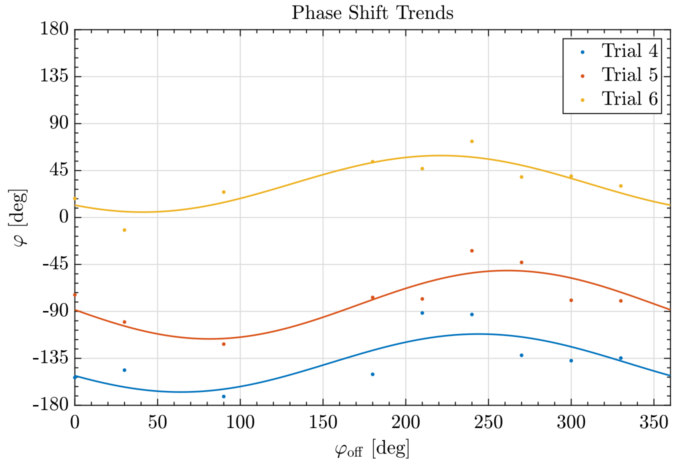

Fig. 13. Estimated wake phase shift versus applied synchronization phase offset φ_{off}, grouped by experimental trial. Each marker corresponds to a steady-state estimate extracted from one case. Different colors represent different trials. A systematic S-shaped trend is visible, indicating that the estimator phase is slightly biased by the applied control offset.

Like in the previous section, the estimated phase signal φ_k for each case was unwrapped and fitted with a linear model over the steady-state interval. The intercept of this fit, representing the steady-state phase shift φ, was then plotted against the applied phase offset φ_{off}, as shown in Fig. 13. However, here we now investigate the effect of φ_{off} on φ, as φ_{off} is varied at each case in the trial. A first harmonic fit was performed to illustrate the variation of the phase shift estimate against the applied offset. Note that the absolute values between trials differ, as discussed earlier.

Interestingly, the estimated φ is not constant across the applied φ_{off}, even though the upstream wake should remain unchanged within each trial. A consistent S-shaped trend is observed, where phase estimates are below average around 70° and above average near 250°. This behavior suggests that the estimator output is influenced by φ_{off} applied to T2 itself. Although the estimator is designed to detect the upstream wake, the cyclic actuation of the downstream turbine modifies the structural response in a nonlinear way. At certain φ_{off}, the control-induced motion either reinforces or partially cancels the wake-induced signal, leading to deviations in the estimated φ. These interactions are not accounted for by the linear Kalman filter model, which assumes additive and independent disturbances (see [33]). As a result, the estimator slightly misattributes the combined response, causing φ estimates to vary slightly with φ_{off}. This denotes a limitation of the current estimator design: it does not model closed-loop interactions between control and wake-induced response, and may have slight bias under feedback. The presence of a bias mainly affects the absolute alignment between estimated and true wake phase, but the estimator consistently preserves the relative phase trends across applied offsets. As a result, synchronization accuracy in terms of aligning turbine response to upstream forcing remains intact, although calibration of the absolute phase may be shifted. The origin of the S-shaped bias is residual model mismatch, which causes part of the control-induced response to be projected onto the periodic state. A detailed frequency-domain derivation interpreting this bias is provided in Appendix B. In future work, this limitation could be mitigated by extending the estimator to explicitly include closed-loop dynamics. Alternatively, measurement channels such as blade-root loads or yaw moments could be added to help decouple wake- and control-induced responses.

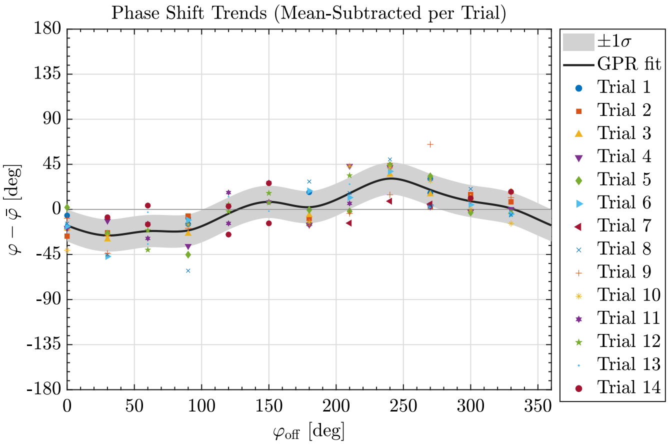

Fig. 14. Mean-subtracted wake phase estimates across trials. For each trial, the average phase shift $\bar{\varphi}$ was removed to highlight the relative dependence on φ_{off}. The solid line shows a Gaussian Process Regression (GPR) model fitted to the data, and the shaded area denotes one standard deviation of posterior uncertainty. The alignment of data across trials confirms repeatability, while the smooth GPR curve emphasizes the consistent bias trend.

To account for the absolute differences between trials, the mean phase shift per trial $\bar{\varphi}$ was subtracted, and the mean-centered results are shown in Fig. 14. Gaussian Process Regression (GPR) [34] was used to model the relationship between the applied phase offset φ_{off} and the estimated phase shift φ, capturing both the underlying trend and the uncertainty due to experimental variability. To reflect the periodic nature of the phase domain, the dataset was augmented with phase-shifted copies at ±360°. The shaded regions in Fig. 14 indicate ±1 standard deviation σ from the GPR posterior. Models were trained using MATLAB's `fitrgp` function (Statistics and Machine Learning Toolbox), with a Matérn 3/2 kernel, standardized inputs. Model fitting was fully automated within the analysis script. The consistent alignment of the individual trials and the smooth GPR trends confirm that the estimator reliably tracks the φ of the imposed offsets.

5.3. Effect of synchronization on turbine performance

This section evaluates how synchronized Helix control affects turbine performance. In all experimental cases, the second turbine (T2) employs the proposed synchronization controller, which estimates φ of the periodic wake generated by the upstream turbine (T1) using a Kalman filter, and synchronizes its actuation accordingly.

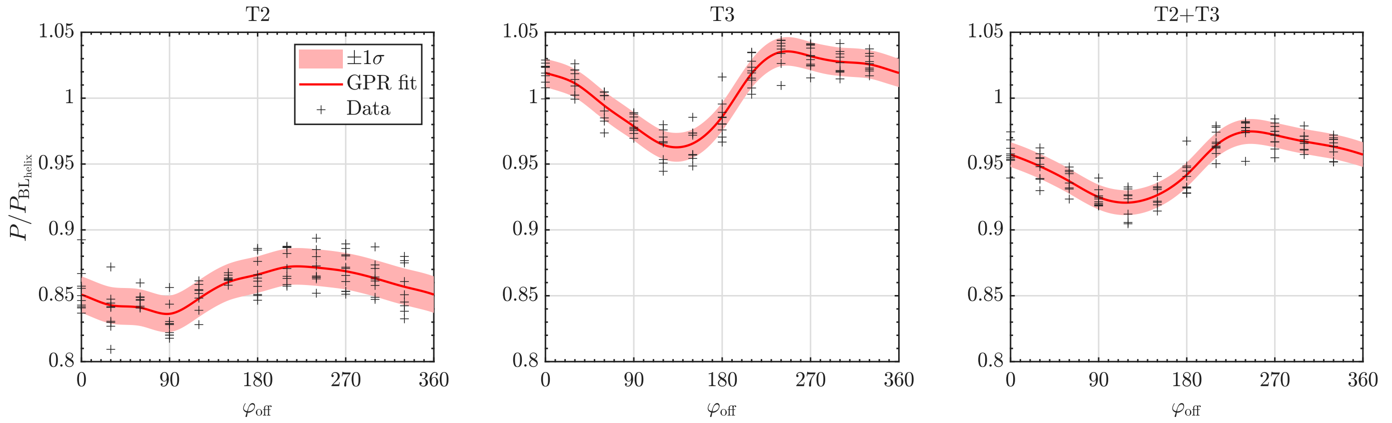

Fig. 15. Normalized power production of turbines T2, T3, and the combined array as a function of applied synchronization phase offset at T2. T1 was held at a fixed Helix setting and therefore omitted. T3 shows a systematic dependence on phase offset, with a maximum gain of about 3% near $\varphi_{\mathrm{off}} \approx 270°$ and a minimum near 120°. T2 consistently experiences an approximate 15% power loss due to unsteady aerodynamic effects of cyclic pitching at model scale. The combined output (T2+T3) does not increase in this setup, but at utility scale, where cyclic losses are negligible, array-level benefits are expected.

To explore the effect of relative wake alignment between the two turbines, a prescribed phase offset φ_{off} is applied to the synchronized control action of T2. That is, the controller enforces actuation of T2 with a fixed phase shift relative to the estimated incoming wake phase, ranging from 0° to 330° in 30° increments. This setup ensures that all performance differences result directly from variations in synchronized phase alignment, while the upstream turbine applies a constant Helix.

Gaussian process regression is used to model the relationship between the applied phase offset and performance indicators. Fig. 15 shows the GPR-modeled power production as a function of the applied phase offset, including ±1 standard deviation σ uncertainty bands from the posterior distribution. Similar settings as in the previous section were used, but here the noise standard deviation was fixed at $\sigma_{\mathrm{noise}} = 0.02$. Turbine 1 applied a constant Helix forcing throughout the experiment, and its power output is unaffected across φ_{off}. It therefore acts as a fixed wake generator, while the relevant array-level variation arises from the trade-off between T2 and T3. For this reason, T1 is not further analyzed in terms of power or loads. Accordingly, we define the combined output of T2+T3 as the relevant array-level metric in this setup.

The third turbine (T3) shows a clear pattern: power increases by about 3% at a φ_{off} near 270°, and drops near 120°. This confirms that the phase difference between T1 and T2 affects how their wakes interact, either amplifying or canceling each other. Interestingly, the exact positions of the peak and dip are not 180° apart, which could be expected from ideal constructive and destructive interference.

T2's power output is consistently about 15% lower than in the baseline helix scenario. This reduction is caused by aerodynamic losses from the continuous pitch motion used for synchronization. As explained in Section 3, although the mean pitch angle remains at its optimal value, the cyclic actuation introduces effects such as lift hysteresis and dynamic stall, which reduce aerodynamic efficiency. These effects are particularly present in small-scale turbines, where the power coefficient curve drops steeply around the optimal value and Reynolds numbers are low. At utility scale, pitch amplitudes are orders of magnitude smaller relative to rotor dynamics, and such unsteady aerodynamic penalties are negligible. As a result, the absolute efficiency losses observed at T2 in this setup should not be directly generalized to full-scale turbines. Instead, the experiments should be viewed as a proof-of-principle demonstration of synchronization, with the main insight being the relative dependence of downstream performance on phase offset rather than the absolute values of turbine efficiency.

The optimal phase offset φ_{off} differs between the wind tunnel experiments and the LES study done in [16,17] due to variations in both the definition of φ_{off} and the estimation approach. In this study, a linear Kalman filter estimates the phase of the periodic wake-induced pitch disturbance on the downstream turbine, and the phase offset is defined relative to this estimated phase. Conversely, the EKF-based approach [16] defines the phase offset as the offset applied to the phase of the estimated periodic wind speed component impinging on the downstream turbine, while [17] determines the downstream wake phase through flow field analysis. These fundamentally different reference frames and estimation methodologies make it non-trivial to back-calculate an absolute phase shift between the approaches. In the current approach, all phase lags introduced by the turbine dynamics between the inflow, wake, and resulting blade loads are implicitly included, whereas the EKF-based approach does not capture these internal dynamics. Given the nonlinear nature of wind turbine behavior, these phase lags are also operating-point dependent (e.g., wind speed and rotor speed). However, all these studies show similar trends, where there are regions of optimal and suboptimal power production, following a characteristic S-curve.

Fig. 16 was created using identical GPR methodology. It shows the magnitude of the power spectrum at the excitation frequency against the applied φ_{off}, which reflects the degree of constructive or destructive interference between the turbine's pitching motion and the periodic incoming wake. Interestingly, the peak in fore–aft strain occurs around 150°, which does not align with the peak in power production at approximately 270°. Instead, it seems that the region of low power production is associated with higher tower-base strain, which aligns with results obtained in the DIC wind tunnel experiment [25]. Also in [21], this behavior is observed for the tower-base load. From that study, note that other components, such as the blades and tower top, experience increased fatigue around the phase offset region of high power production. This shows that the phase offset giving the highest power production is different from the one that minimizes structural loading, suggesting that future control strategies need to balance both objectives.

6. Conclusion

This study introduced and experimentally validated a synchronization control scheme aimed at leveraging periodic wake structures caused by upstream turbines to enhance the performance of downstream turbines. The control methodology extends previous theoretical work by incorporating a Kalman-filter-based phase estimation algorithm tailored specifically for wind turbine applications, employing the MBC framework for integration with individual pitch control.

Experimental validation conducted on a scaled three-turbine wind farm setup in a controlled wind tunnel environment demonstrated

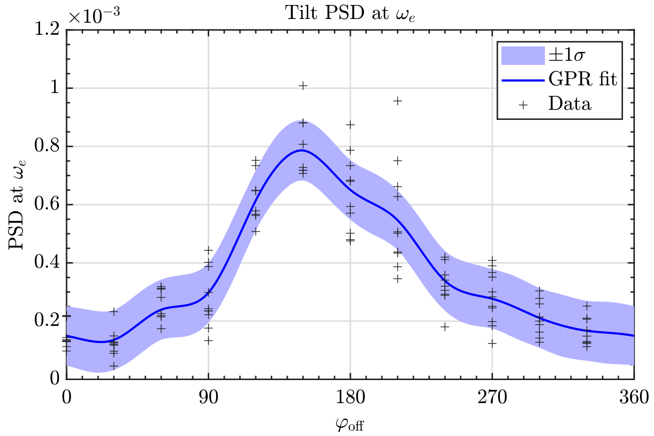

Fig. 16. Magnitude of the tower-base strain spectrum at the excitation frequency ω_e as a function of synchronization phase offset φ_{off}. Solid line shows a Gaussian Process Regression (GPR) fit with shaded one-standard-deviation uncertainty bands. Peaks indicate constructive interference between wake-induced and control-induced loading, while troughs indicate partial cancellation. Notably, the load maximum occurs at a different phase offset than the power maximum (Fig. 15), illustrating a trade-off between maximizing energy capture and minimizing structural loading in synchronized wake control.

the estimator's capability to consistently and accurately track periodic wake structures generated upstream. The evaluation of different synchronization phase offsets revealed a dependency of downstream turbine performance on the imposed phase difference. The optimal phase offset for maximizing energy production at the third turbine resulted in a power gain of approximately 3% on the third turbine compared to a baseline Helix scenario without synchronization. Interestingly, the experimentally observed peak and dip in T3 production are not 180° apart. We hypothesize that non-ideal interference and operating point-dependent phase lags contribute to this shift. Quantifying these lags and their dependence on operating conditions is a direction for future work. The actuating turbine (T2) experienced a power decrease of about 15% due to small-scale unsteady aerodynamic effects associated with cyclic pitching at the high actuation frequencies of the model turbines. Importantly, when considering total array production, T1 acted as a fixed wake generator with constant output, so the relevant variation arises from T2 and T3. Their combined output did not show a systematic increase over the baseline Helix case, as losses at T2 generally outweighed gains at T3 in this small-scale setting; at utility scale, where cyclic pitch amplitudes and associated losses are much smaller, array-level benefits are expected to be more significant, as demonstrated in simulations in earlier work.

The experimental scope has several limitations that provide context for the interpretation of these results: (i) no blade load sensors were available, preventing advanced blade-element modeling in the estimator; (ii) a linear Kalman filter relying solely on tower-base fore–aft strain was employed, which limits the operating range; (iii) the current estimator design does not explicitly model closed-loop interactions between downstream actuation and measured response, which introduced a small phase-estimation bias that varied with the applied offset; (iv) all experiments were conducted around a fixed operating point (constant wind speed, fixed mean pitch angle) with periodic forcing at a single frequency, so variability across operating conditions and varying frequencies is not examined; (v) scaling limitations inherent to wind tunnel models restrict direct extrapolation of absolute performance values to full-scale turbines, and the findings should primarily be interpreted in terms of relative phase–performance trends; and (vi) the narrow sensor suite restricted validation to tower-base fore–aft strain only, preventing assessment of yaw-related and blade-root loads, so the estimator–controller framework was demonstrated in a simplified SISO setting rather than its full multivariable form.

The findings from the wind tunnel also have broader implications for wind farm control. In large offshore arrays, where multiple turbines are persistently exposed to wakes, the ability of downstream turbines to synchronize with upstream-induced periodic structures may provide a means to improve array-level performance. The experiments show that downstream power depends sensitively on the relative phase alignment, indicating that coordinated synchronization across several turbines could enhance overall farm efficiency beyond what is achieved with conventional methods. At the same time, the observed difference between the phase offsets that maximize power and those that reduce structural loading stresses the need for multi-objective control approaches that consider both power production and fatigue life. These results suggest that synchronization can complement existing strategies as wind farms become larger and more densely packed.

Future work could explore nonlinear or adaptive modeling approaches to enhance estimation robustness under dynamic control conditions, explicitly address closed-loop coupling in the observer, and incorporate blade load sensing to enable more advanced models. In addition, full-scale field tests and extensive numerical simulations should evaluate multi-objective, array-level control that balances total production and structural loading across turbines beyond a single operating point.

CRediT authorship contribution statement

Aemilius A.W. van Vondelen: Writing – review & editing, Writing – original draft, Visualization, Validation, Software, Project administration, Methodology, Investigation, Formal analysis, Data curation, Conceptualization. **Daan C. van der Hoek:** Writing – review & editing, Supervision, Software, Resources, Investigation. **Sachin T. Navalkar:** Writing – review & editing, Supervision. **Jan-Willem van Wingerden:** Writing – review & editing, Supervision, Resources, Funding acquisition.

Declaration of competing interest

The authors declare the following financial interests/personal relationships which may be considered as potential competing interests: J.W. van Wingerden reports financial support was provided by Crosswind C.V. A.A.W. van Vondelen reports financial support was provided by Siemens Gamesa Renewable Energy B.V. A.A.W. van Vondelen reports a relationship with Siemens Gamesa Renewable Energy BV that includes: non-financial support. A.A.W. van Vondelen has patent #NL2035238B1 issued to Crosswind Beheer B V. If there are other authors, they declare that they have no known competing financial interests or personal relationships that could have appeared to influence the work reported in this paper.

Acknowledgments

This work is part of the Hollandse Kust Noord wind farm innovation program where CrossWind C.V., Shell, Eneco, Grow, and Siemens Gamesa are teaming up. Funding for the PhDs was provided by CrossWind C.V. and Siemens Gamesa. We would further like to acknowledge Wim Wien, Ralph Willekes, Will van Geest, and Tristan Crumpton for their invaluable help with preparing the experimental setup.

Appendix A. Details on system identification and tuning

The proposed Kalman-filter-based synchronization control scheme requires an accurate system model to reliably estimate the periodic wake disturbances. Although wind turbines are inherently nonlinear, linear system identification is frequently employed in practice due to its relative simplicity and computational efficiency. However, linear models are typically only accurate around their specific operating points, which means that a different model may be required for other operating conditions (e.g., wind speeds, rotor speeds).

Identification procedure

To identify a suitable linear model, input–output data were collected at steady-state conditions using pseudo-random binary noise (PRBN) applied to the tilt control input for 30 min. The PRBN excitation frequency content extended up to 6 Hz, surpassing the actuator bandwidth of about 5 Hz, ensuring persistent excitation within the relevant frequency range. The turbine response was measured using the tower-bottom fore–aft strain gauge (see Fig. 5).

Before identification, the data were preprocessed to remove biases and high-frequency noise. Specifically, the data were mean-centered, detrended, and resampled from the original sampling frequency of 2 kHz to 25 Hz (factor of 80 reduction) to focus identification on the low-frequency dynamics most relevant for synchronized wake control.

The identification procedure employed the optimal predictor-based subspace identification method (PBSID$_{\text{opt}}$) as described in [35], due to its robustness and suitability for linear system identification from noisy data.

Model order selection and validation

The selection of the appropriate system order is critical to ensure that the model accurately captures the essential system dynamics without unnecessary complexity. Singular value decomposition (SVD) of the Hankel matrix was initially performed, but it provided no definitive indication of an optimal model order. Therefore, a model set with orders ranging from 3 to 10 was evaluated based on frequency-response fits.

A 5-state model emerged as the most appropriate choice, as lower-order models inadequately captured the resonances, whereas higher-order models only provided marginal improvements while introducing complexity.

The accuracy of the selected 5-state model was validated by comparing its frequency response with the measured experimental data, as illustrated in Fig. 9. The model accurately represents the system behavior in the frequency range crucial for the wake mixing control experiments (approximately 0.2 Hz to 5 Hz), particularly around the wake excitation frequency ($f_{\text{e}} \approx$ 1–3 Hz). Minor discrepancies are present above 5 Hz, but these frequencies are outside the band of interest for wake mixing control.

Final identified model

The final discrete-time linear state-space model used in the Kalman-filter implementation is represented as:

$$x_{k+1} = A_{\text{d}} x_k + B_{\text{d}} u_k + w_k, \tag{A.1}$$

$$y_k = C_{\text{d}} x_k + D_{\text{d}} u_k + v_k, \tag{A.2}$$

where matrices $\{A_{\text{d}}, B_{\text{d}}, C_{\text{d}}, D_{\text{d}}\}$ were obtained from the optimal PBSID identification procedure. Process noise w_k and measurement noise v_k are modeled as zero-mean white Gaussian sequences with finite covariance.

In the identified model, the input $u_k \in \mathbb{R}$ corresponds to the tilt control command (Eq. (16)) applied to the second turbine. The output $y_k \in \mathbb{R}$ is the measured fore–aft tower-base strain, which serves as a proxy for the tilt moment (Eq. (20)). Thus, the identified system is single-input, single-output (SISO), consistent with the actuation and sensing architecture described in Section 3. Although the full multi-blade system is inherently multivariable, only the tilt input and response are considered for identification, as this mode directly captures the periodic loading used for phase estimation. This choice is motivated by the availability of strain sensing and the orthogonality of the tilt and yaw axes, as discussed in Section 2.2.

This linear model was subsequently augmented with the periodic disturbance states and integrated into the Kalman-filter-based synchronization control framework for experimental evaluation. The number of periodic components in the disturbance model is set to $h = 1$, corresponding to the known Helix excitation frequency ω_{e}. The disturbance state vector $x_p(t) \in \mathbb{R}^{2h}$ therefore has dimension 2, capturing the in-phase and quadrature components (i.e., sine and cosine) of this single frequency. While the framework allows for multiple periodic inputs with arbitrary frequencies ω_i, only a single component is used in the current experiments due to the upstream wake excitation with ω_{e}.

Kalman filter tuning

The Kalman filter is initialized with zero state estimates and an identity matrix for the error covariance. To ensure consistent convergence across experimental repetitions, the filter state and covariance are reset at the start of each new case. This is triggered using a pulse signal that rises from 0 to 1 on the first timestep of a new case. On this rising edge, both the state estimate and the error covariance matrix are reinitialized. This prevents residual estimation errors or phase lag from persisting across cases, which is especially important when comparing performance across different control phase offsets.

The process and measurement noise covariances were tuned heuristically by evaluating performance across multiple trials. In this context, performance refers to the consistency and accuracy of the estimated wake phase, as validated by repeatability in open-loop experiments (see Section 5.1) and by the correlation between estimated phase offsets and downstream power production trends (Section 5.3). Lower process noise was assigned to the identified states, while the augmented periodic disturbance states were given adjustable noise levels to balance phase tracking sensitivity and robustness. Measurement noise was set conservatively low to reflect the high precision of the available sensor data. Tuning parameters were iteratively adjusted to minimize phase estimation drift and ensure stable convergence across repeated experiments, without the use of a formal optimization procedure.

Appendix B. Detailed interpretation of estimator bias

To interpret the estimator bias, let us analyze the estimator output at the excitation frequency $\omega = \omega_{\text{e}}$. The response of the strain gauge can be expressed in the frequency domain as:

$$Y(\text{j}\omega) = G_{\text{c}}(\text{j}\omega)\, U^{\text{c}} + G_{\text{w}}(\text{j}\omega)\, U^{\text{p}}, \tag{B.1}$$

with $U^{\text{c}} = A_{\text{c}} e^{\text{j}\phi_c}$ the applied control phasor and $U^{\text{p}} = A_{\text{w}} e^{\text{j}\phi_w}$ the upstream wake phasor. The model used in the Kalman filter predicts:

$$\hat{Y}(\text{j}\omega) = \hat{G}_{\text{c}}(\text{j}\omega)\, U^{\text{c}} + \hat{G}_{\text{w}}(\text{j}\omega)\, \hat{U}^{\text{p}}. \tag{B.2}$$

Any mismatch between the identified model and the real system $\Delta G_c = G_c - \hat{G}_c$ contributes to a residual between the measured and predicted output, i.e., the innovation of the Kalman filter, which the filter projects onto the periodic state, because in the SISO implementation we have $V = 1$, as such $B^{\text{p}} = B^{\text{c}}$ and $D^{\text{p}} = D^{\text{c}}$. As a result, the residual cannot be distinguished from the periodic disturbance, and it is partially projected onto the periodic state estimate. This channel alignment was chosen deliberately to avoid having to identify the true disturbance pathway. While this simplifies implementation, it also implies that the filter cannot cleanly separate control-induced and wake-induced dynamics in the case of model mismatch. At steady state, this model mismatch propagates as:

$$\hat{U}^{\text{p}} \approx U^{\text{p}} + H(\omega)\, \Delta G_c(\omega)\, U^{\text{c}}, \tag{B.3}$$

where, $H(\omega)$ represents the frequency-dependent mapping from innovation to the disturbance state that arises from the Kalman filter update. Writing $H(\omega)\Delta G_c(\omega) = |B| e^{\text{j}\delta}$ yields:

$$\hat{U}^{\text{p}} = A_w e^{\text{j}\phi_w} + |B| A_c e^{\text{j}(\phi_c + \delta)}, \tag{B.4}$$

where $|B|$ is the magnitude of the bias contribution and δ is its phase angle. The estimated phase, therefore, becomes:

$$\hat{\phi} - \phi_w = \arg\Big(1 + \rho e^{\text{j}(\varphi_{\text{off}} + \delta)}\Big), \qquad \rho = \frac{|B| A_c}{A_w}, \tag{B.5}$$

which is the argument of a two-vector phasor sum. As $\varphi_{\mathrm{off}} = \phi_c - \phi_w$ is varied, this relation yields the characteristic S-shaped trend seen in Fig. 13. In the ideal case $\Delta G_c = 0$, the bias term vanishes and $\hat{\phi} = \phi_w$, independent of φ_{off}.

References

[1] M. Baricchio, P.M.O. Gebraad, J.W. van Wingerden, Evaluating the potential of a wake steering co-design for wind farm layout optimization through a tailored genetic algorithm, Wind. Energy Sci. 9 (11) (2024) 2113–2132, http://dx.doi.org/10.5194/wes-9-2113-2024, URL https://wes.copernicus.org/articles/9/2113/2024/.

[2] R.J. Stevens, C. Meneveau, Flow structure and turbulence in wind farms, Annu. Rev. Fluid Mech. 49 (2017) 311–339, http://dx.doi.org/10.1146/annurev-fluid-010816-060206.

[3] F. González-Longatt, P. Wall, V. Terzija, Wake effect in wind farm performance: Steady-state and dynamic behavior, Renew. Energy 39 (1) (2012) 329–338.

[4] R.J. Barthelmie, K. Hansen, S.T. Frandsen, O. Rathmann, J.G. Schepers, W. Schlez, J. Phillips, K. Rados, A. Zervos, E.S. Politis, P.K. Chaviaropoulos, Modelling and measuring flow and wind turbine wakes in large wind farms offshore, Wind. Energy 12 (5) (2009) 431–444, http://dx.doi.org/10.1002/we.348, arXiv:https://onlinelibrary.wiley.com/doi/pdf/10.1002/we.348 URL https://onlinelibrary.wiley.com/doi/abs/10.1002/we.348.

[5] J. Meyers, C. Bottasso, K. Dykes, P. Fleming, P. Gebraad, G. Giebel, T. Göçmen, J.W. van Wingerden, Wind farm flow control: prospects and challenges, Wind. Energy Sci. 7 (6) (2022) 2271–2306, http://dx.doi.org/10.5194/wes-7-2271-2022, URL https://wes.copernicus.org/articles/7/2271/2022/.

[6] J. Annoni, P.M. Gebraad, A.K. Scholbrock, P.A. Fleming, J.W.v. Wingerden, Analysis of axial-induction-based wind plant control using an engineering and a high-order wind plant model, Wind. Energy 19 (6) (2016) 1135–1150.

[7] D. van der Hoek, S. Kanev, J. Allin, D. Bieniek, N. Mittelmeier, Effects of axial induction control on wind farm energy production-a field test, Renew. Energy 140 (2019) 994–1003.

[8] P.A. Fleming, P.M. Gebraad, S. Lee, J.W. van Wingerden, K. Johnson, M. Churchfield, J. Michalakes, P. Spalart, P. Moriarty, Evaluating techniques for redirecting turbine wakes using SOWFA, Renew. Energy 70 (2014) 211–218.

[9] S. Gamesa, Siemens gamesa now able to actively dictate wind flow at offshore wind locations, 2019, URL https://www.siemensgamesa.com/en-int/newsroom/2019/11/191126-siemens-gamesa-wake-adapt-en. (Accessed 13 September 2025).

[10] J.P. Goit, J. Meyers, Optimal control of energy extraction in wind-farm boundary layers, J. Fluid Mech. 768 (2015) 5–50.

[11] J.A. Frederik, J.W. van Wingerden, On the load impact of dynamic wind farm wake mixing strategies, Renew. Energy 194 (2022) 582–595, http://dx.doi.org/10.1016/j.renene.2022.05.110, URL https://www.sciencedirect.com/science/article/pii/S0960148122007613.

[12] J.A. Frederik, B.M. Doekemeijer, S.P. Mulders, J.W. van Wingerden, The helix approach: Using dynamic individual pitch control to enhance wake mixing in wind farms, Wind. Energy 23 (8) (2020) 1739–1751, http://dx.doi.org/10.1002/we.2513.

[13] D.C. van der Hoek, B. Van den Abbeele, C.S. Ferreira, J.-W. van Wingerden, Maximizing wind farm power output with the Helix Approach: Experimental validation and wake analysis using tomographic PIV, Wind. Energy 27 (5) (2024) 463–482, http://dx.doi.org/10.1002/we.2896.

[14] A.A.W. van Vondelen, S.T. Navalkar, D.R.H. Kerssemakers, J.W. van Wingerden, Enhanced wake mixing in wind farms using the Helix approach: A loads sensitivity study, in: 2023 American Control Conference, ACC, 2023, pp. 831–836, http://dx.doi.org/10.23919/ACC55779.2023.10155965.

[15] E. Taschner, A.A.W. van Vondelen, R. Verzijlbergh, J.W. van Wingerden, On the performance of the helix wind farm control approach in the conventionally neutral atmospheric boundary layer, 2505, (1) IOP Publishing, 2023, 012006, http://dx.doi.org/10.1088/1742-6596/2505/1/012006,

[16] A.A.W. van Vondelen, A.K. Pamososuryo, S.T. Navalkar, J.W. van Wingerden, Control of periodically waked wind turbines, IEEE Trans. Control Syst. Technol. 33 (2) (2025) 700–713, http://dx.doi.org/10.1109/TCST.2024.3508577.

[17] H. Korb, H. Asmuth, S. Ivanell, The characteristics of helically deflected wind turbine wakes, J. Fluid Mech. 965 (2023) A2, http://dx.doi.org/10.1017/jfm.2023.390.

[18] A.A.W. van Vondelen, J. Ottenheym, A.K. Pamososuryo, S.T. Navalkar, J.W. van Wingerden, Phase synchronization for Helix enhanced wake mixing in downstream wind turbines, IFAC-PapersOnLine 56 (2) (2023) 8426–8431, http://dx.doi.org/10.1016/j.ifacol.2023.10.1039, URL https://www.sciencedirect.com/science/article/pii/S2405896323014416, 22nd IFAC World Congress.

[19] E. Simley, L.Y. Pao, Evaluation of a wind speed estimator for effective hub-height and shear components, Wind. Energy 19 (1) (2016) 167–184.

[20] T. Knudsen, T. Bak, M. Soltani, Prediction models for wind speed at turbine locations in a wind farm, Wind. Energy 14 (7) (2011) 877–894.

[21] A.A.W. van Vondelen, M. Coquelet, S.T. Navalkar, J.W. van Wingerden, Synchronized Helix wake mixing control, Wind. Energy Sci. 10 (10) (2025) 2411–2433, http://dx.doi.org/10.5194/wes-10-2411-2025.

[22] M. Mancini, J. Schreiber, C.A. Bottasso, Closed-loop wake redirection in wind tunnel experiments, Wind. Energy Sci. 8 (2) (2023) 431–450, http://dx.doi.org/10.5194/wes-8-431-2023.

[23] J. Schreiber, C.A. Bottasso, Experimental validation of wind farm wake steering strategies, Renew. Energy 195 (2022) 319–331, http://dx.doi.org/10.1016/j.renene.2022.05.111.

[24] D. van der Hoek, J.A. Frederik, M. Huang, F. Scarano, C. Simão Ferreira, J.W. van Wingerden, Experimental analysis of the effect of dynamic induction control on a wind turbine wake, Wind. Energy Sci. 7 (3) (2022) 1305–1320, http://dx.doi.org/10.5194/wes-7-1305-2022.

[25] A.A.W. van Vondelen, D.C. van Der Hoek, S.T. Navalkar, J.W. van Wingerden, Synchronized dynamic induction control: An experimental investigation, 2767, (3) IOP Publishing, 2024, 032027, http://dx.doi.org/10.1088/1742-6596/2767/3/032027,

[26] G. Bir, Multi-blade coordinate transformation and its application to wind turbine analysis, in: 46th AIAA Aerospace Sciences Meeting and Exhibit, 2008, p. 1300.

[27] M. Verhaegen, V. Verdult, Filtering and System Identification: a Least Squares Approach, Cambridge University Press, 2007.

[28] L.E.M. Lignarolo, D. Ragni, F. Scarano, C.J. Simão Ferreira, G.J.W. van Bussel, Tip-vortex instability and turbulent mixing in wind-turbine wakes, J. Fluid Mech. 781 (2015) 467–493, http://dx.doi.org/10.1017/jfm.2015.470.

[29] J. Schottler, A. Hölling, J. Peinke, M. Hölling, Design and implementation of a controllable model wind turbine for experimental studies, in: Journal of Physics: Conference Series, Vol. 753, IOP Publishing, 2016, 072030.

[30] W.J. McCroskey, Unsteady Airfoils, NASA Technical Memorandum NASA-TM-81182, NASA Ames Research Center, Moffett Field, CA, 1982.

[31] C.J. O'Rourke, M.M. Qasim, M.R. Overlin, J.L. Kirtley, A geometric interpretation of reference frames and transformations: dq0, Clarke, and Park, IEEE Trans. Energy Convers. 34 (4) (2019) 2070–2083.

[32] D. van der Hoek, J. Frederik, M. Huang, F. Scarano, C. Simao Ferreira, J.W. van Wingerden, Experimental analysis of the effect of dynamic induction control on a wind turbine wake, Wind. Energy Sci. 7 (3) (2022) 1305–1320.

[33] M. Coquelet, M. Lejeune, L. Bricteux, A.A.W. van Vondelen, J.W. van Wingerden, P. Chatelain, On the robustness of a blade load-based wind speed estimator to dynamic pitch control strategies, Wind. Energy Sci. 9 (10) (2024) 1923–1940, http://dx.doi.org/10.5194/wes-9-1923-2024, https://wes.copernicus.org/articles/9/1923/2024/.

[34] C.E. Rasmussen, C.K.I. Williams, Gaussian Processes for Machine Learning, MIT Press, Cambridge, MA, 2006, URL http://www.gaussianprocess.org/gpml/.

[35] A. Chiuso, The role of vector autoregressive modeling in predictor-based subspace identification, Automatica 43 (6) (2007) 1034–1048.